



# Coherent x-ray diffractive imaging of a bent GaN nanowire

Vladimir Ladygin

*Moscow Institute of Physics and Technology, Moscow, Russia*

Supervisors: Young Yong Kim, Ivan Vartaniants

*DESY, Hamburg, Germany*

# Abstract

GaN nanowires (NWs) are promising building blocks for future optoelectronic devices and nanoelectronics. They exhibit stronger piezoelectric properties than bulk GaN. These phenomena may be crucial for applications of NWs and makes their study highly important. The structural changes were investigated using Bragg diffraction with coherent x-ray.

The structural properties of NWs were reflected in the three-dimensional (3D) intensity distribution. The phase shifting related to the displacement by bending of NWs was significantly affect to the diffraction pattern. This bending was observed under applied voltage bias.

The reconstruction of object was performed using Bragg coherent X-ray diffraction imaging (BCDI). This method revealed the information of displacement of bending structure. However, the empty gaps in structure was investigated from a certain value of displacement.

To exploit this problem of reconstruction, we employed a finite element method (FEM) approach for analytical simulations based on elasticity theory. After obtaining 3D diffraction pattern by the Fourier transform from simulated NWs as changing displacement, phase retrieval method was used for the reconstruction. By changing the displacement gradually, we figured out the starting point to show the gaps in reconstruction object.

Our demonstration showed the criteria of limitation from displacement in reconstruction.

## Contents

## 1. Introduction

Semiconductor nanowires (NWs) based on gallium nitride (GaN), indium nitride (InN), and indium gallium nitride (InGaN) have promising applications for light-emitting diodes, low-cost solar cells, transistors, single photon sources, and other devices [1-6]. The wurtzite (WZ) (hexagonal) crystal structure of GaN NWs is noncentrosymmetric and has an internal electric field along the [0001] crystallographic direction [7,8]. Local deformation of the GaN unit cell leads to formation of an internal piezoelectric field and vice versa [9]. Nitride-based light-emitting diodes (LEDs) grown on c-plane GaN substrate usually show the blue shifts with increased injected current. This effect is usually attributed to the screening of the piezoelectric field when the injected electron density is high, which balances the bending. It was also demonstrated that a single GaN NW exhibits stronger piezoelectricity [10] than a bulk GaN [11]. Integration of the NWs into an electric circuit by metallic contacts may induce additional strain and, therefore, may lead to additional piezoelectric effects in the structure. This may dramatically influence electron−hole pair recombination and alter the efficiency of optoelectronic devices based on GaN NWs [12]. Moreover, better knowledge of the relation between piezoelectric effect and strain field in single GaN NWs with the sizes of hundreds of nanometers could potentially contribute to understanding of inefficient recombination of electron−hole pairs in quantum wells [13−15]. Therefore, investigation of the influence of applied voltages on the structure of a single GaN NW is significantly important.

In this research, we characterized structural information from Bragg coherent x-ray scattering method as well as observed of the criteria from displacement changes were crucial information for method development.

## 2.Sample

The samples were provided by the NanoLund Laboratory at Lund University, Sweden. The GaN NWs with a diameter of 350−400 nm and a length 3−4 μm were grown on a 1 μm thick GaN template on top of a Si (111) substrate using metal organic vapor phase epitaxy (MOVPE) [32]. GaN nanowires with dimensional parameters is shown in Figure 1. The structure of NWs was expected to be pure WZ without dislocations and stacking faults. After the growth, GaN NWs were removed from the original GaN/Si substrate and deposited on a Si (111) chip with a 100 nm thermally grown SiO2 layer on top, as an insulating layer.

Further, 220 nm thick metallic contacts were deposited to connect the ends of single NWs to the pads using electron beam lithography and thermal evaporation of Ti and Au. First a 20 nm thick layer of Ti was deposited on SiO2 and GaN NW to provide good adhesion between Au and GaN, and then 200 nm thick layer of Au on top of Ti layer.

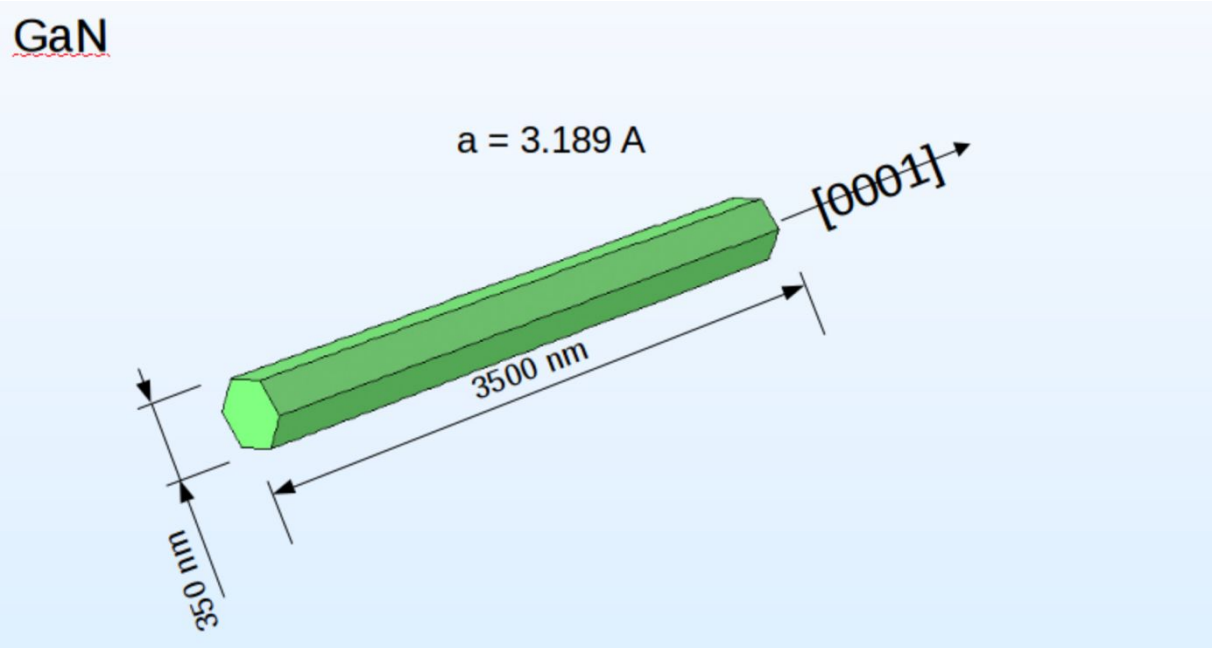


**Figure 1.** Schematic of the GaN nanowire. The lattice constant a = 3.189 A is the unit cell lattice constant of the nanowire in $[10\bar{1}0]$ crystallographic direction.

## 3. Methods

### 3.1. Experimental setup

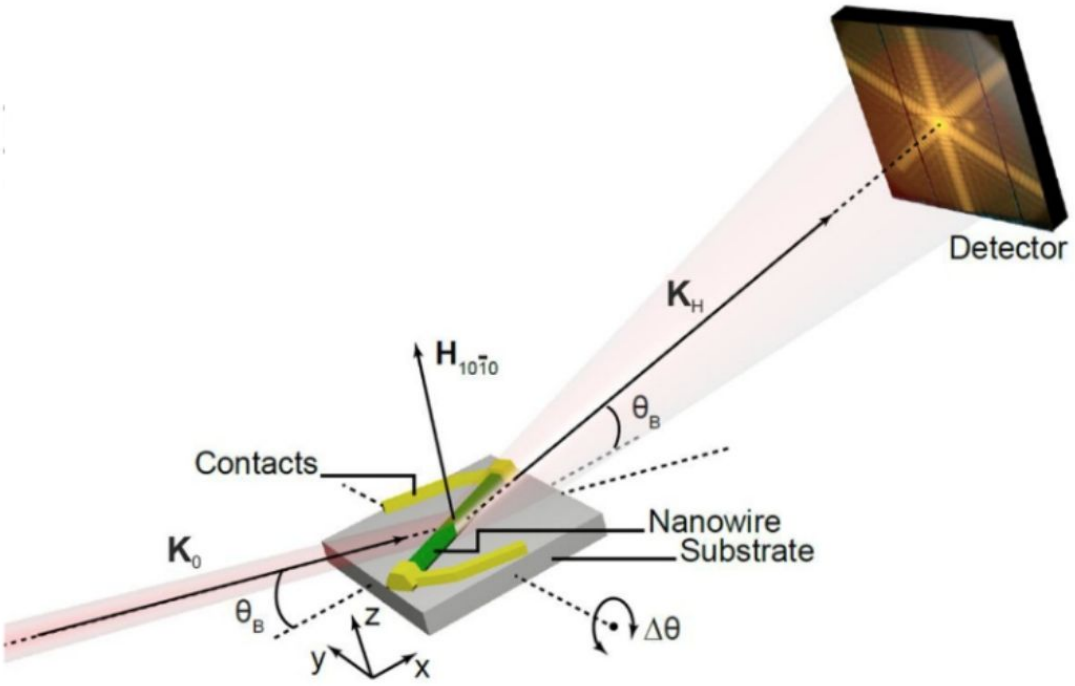


**Figure 2.** Schematic of the diffraction experiment. Detector was placed 1.96 m from the sample. The incoming x-ray beam $K_0$ is scattered by a GaN NW at the Bragg angle $\theta_B$ and resulting diffraction pattern is recorded by the 2D detector in the far-field. $K_H$ wavevector of the reflected beam, $\Delta\theta$ - angular scanning interval.

The experiment was performed at the coherence beamline P10 at the PETRA III synchrotron facility (DESY, Hamburg, Germany). The geometry of the experiment is presented in Figure 2. The x-ray beam with photon energy of 9.6 keV and flux of about $10^{11}$ ph/s was focused at the sample down to one micrometer in size at full width at half-maximum (FWHM) using compound refractive lenses. Characterization of the focus was performed by knife edge scan at the sample position. The measurements were performed at the six-circle diffractometer. It was equipped with a two-dimensional (2D) x-ray pixel detector Lambda (pixel size of 55 × 55 $\mu m^2$) positioned at a distance of 1.96 m from the sample in Bragg geometry. An evacuated flight tube was mounted between the sample and detector to reduce air scattering. The sample

with GaN NWs was mounted on the diffractometer using an adapter with wires connected to a power supply providing bias voltage. The experimental setup allowed measurements of $10\bar{1}0$ Bragg reflection of GaN with the reciprocal lattice vector $H10\bar{1}0$ being normal to the substrate (see Figure 2). After the x-ray beam was positioned at the center of the NW, the rocking curve scan was performed in the angular range of ±0.4° in the vicinity of the Bragg angle with 160 angular steps. At each angular position diffraction patterns were recorded with an exposure time of 20 s.

### 3.2. Coherent X-ray diffraction (CXDI)

Different methods may be employed to reveal structural changes in NWs under applied voltage such as scanning electron microscopy (SEM) or transmission electron microscopy (TEM) [16]. X-ray nanodiffraction, developed recently at synchrotron sources, is an alternative approach that allows one to determine structural properties of single NWs in a nondestructive way [17−20]. Unfortunately, resolution of this method is limited by the x-ray beam size. Newly developed x-ray coherent scattering methods such as Bragg coherent x-ray diffractive imaging (BCDI) and ptychography [21−24] allow to determine strain and deformation of single nanostructures with the spatial resolution reaching 10 nm [25−30]. Moreover, these techniques allow nondestructive investigation of nanostructures in situ and in operando [31]. In this work, we applied BCDI to investigate the influence of bending of a single GaN NW. The general part of this techniques is the phase retrieval algorithm, which is presented in Figure 3. First, we investigated a free-lying NW. It was reconstructed by combination of Hybrid Input-Output [32] and Error reduction algorithms [33] with random initial guess of the phase. Support was defined by the shrink wrap method by updating result after each ten iterations with a threshold value of 0.06 and Gaussian filtering of the support with the sigma value from 2 to 0.1. The final support was given by the hexagonal shape of the NW and Gaussian shape of the illumination function.

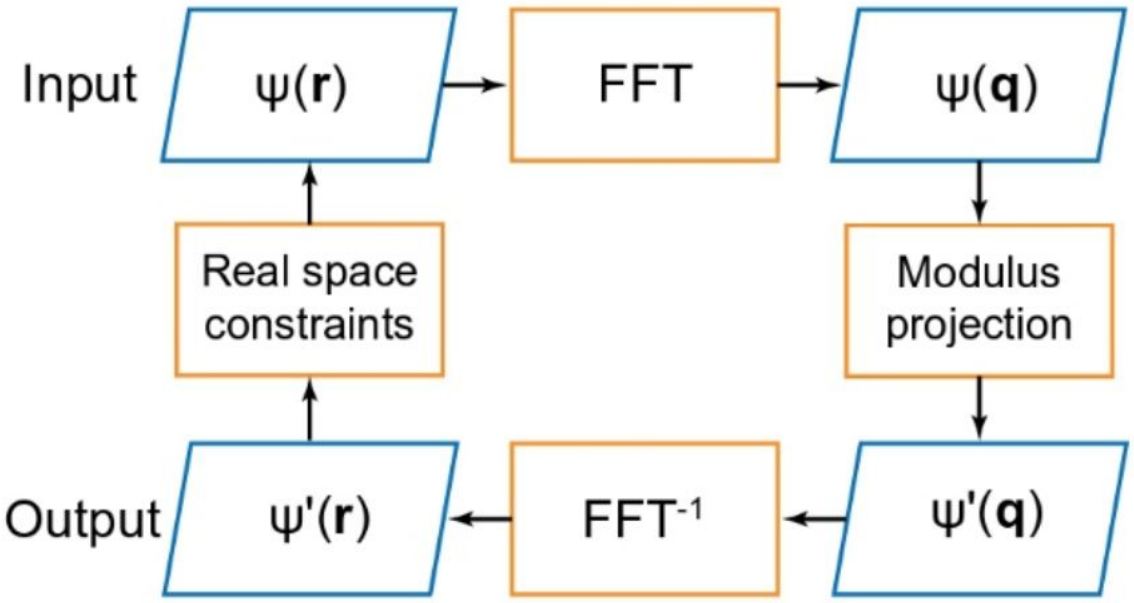


**Figure 3.** Schematic of the phase retrieval algorithm. FFT is a fast Fourier transform. $\psi(q)$ is object function in reciprocal space, $\psi(r)$ – object function in real space.

### 3.3. Finite element method (FEM)

The bending of the GaN NW is the major observations in this research. Taking into account the diameter to length ratio of the NW (1:10), we consider it as a thin rod. The displacement of a thin rod is characterized by a displacement amplitude $u_z(x)$. In our experiment, this displacement is in the direction perpendicular to the surface of the substrate along z-axis. The amplitude $u_z(x)$ is described, in the absence of any shear force, a small displacement, and neglecting a possible initial tilt of the NW, by an elastic equilibrium equation

$$u_x''' = 0, \tag{1}$$

where the prime is denoted to the derivative over the coordinate, and is along the x-axis.

The metallic contacts define boundary conditions of the $u_z(x)$ function

$$u_z(0) = 0,\ u_z(l) = 0. \tag{2}$$

From the asymmetry of the measured x-ray scattered intensity distribution in reciprocal space asymmetric solution of the function $u_z(x)$ is expected. The only nonzero asymmetric solution of the Eq. 1 could be derived if the derivative from one side of the NW

equals to zero and is non-zero from another side. Therefore, these additional boundary conditions, taking into account small angle between the substrate and the GaN NW $tg\alpha \approx \alpha$, could be written as

$$u'_z(l) = 0,\ u'_z(0) = tg\alpha \approx \alpha. \quad (3)$$

The boundary conditions in Eq. 3 are, probably, organized by the geometry of the metallic contacts and the GaN NW is clamped fixed from one side and hinge joint from another. Solution of the differential equation is

$$u_z(x) = u_0 \cdot \left[\left(\frac{x}{l}\right)^3 - 2\left(\frac{x}{l}\right)^2 + \left(\frac{x}{l}\right)\right]. \quad (4)$$

where $u_0 = 27u_{max}/4$ and $u_{max}$ is the maximum of the function $u_z(x)$. The function $u_z(x)$ is presented in Figure 4. From the analytical solution of the elasticity equation for a thin rod $u_z(x)$ length $l(V)$ of the bent NW could be determined as

$$l(V) = \int_0^l \sqrt{1 + u'_z(x)}dx. \quad (5)$$

Interestingly, the maximum $u_{max}$ of the function $u_z(x)$ is located at $x_{max} = l/3$. Angle $\alpha$ is connected to maximal displacement by the equation

$$u_{max} = u\left(\frac{2}{3}l\right) = \frac{4l}{27}tg\alpha. \quad (6)$$

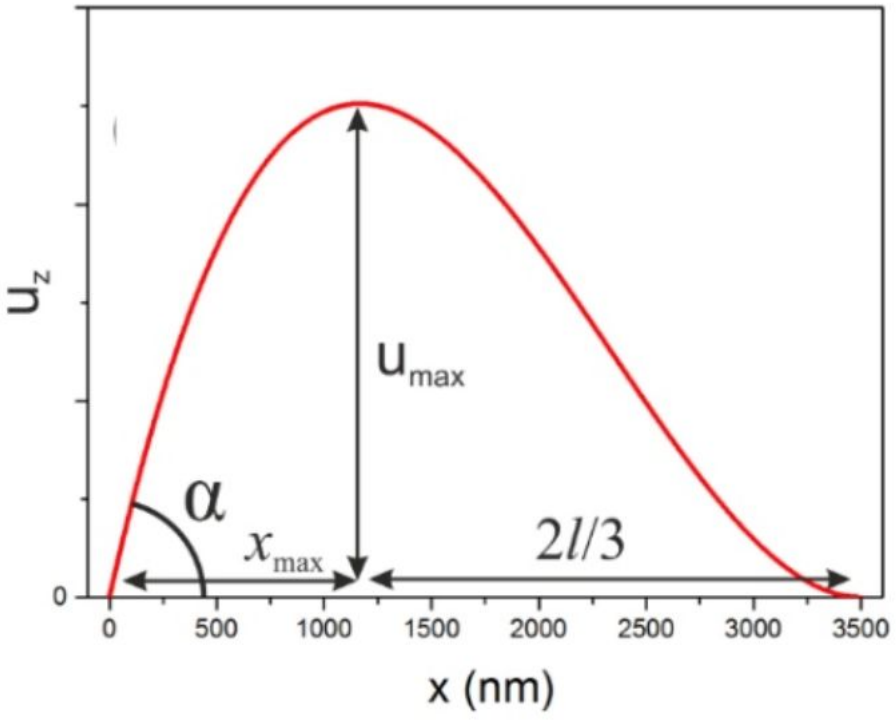

**Figure 4.** Function of the displacement component $u_z$ distribution along x direction of the nanowire in the FEM model.

To study the inner structure of the bending GaN NW, Finite Element Method (FEM) analysis was performed supported by analytical calculations described above. The NW was modeled with the dimensions determined from the SEM studies such as the size between opposite facets equal to $d = 350\,nm$ and the length $l = 3.5\,\mu m$. The analytically derived function $u_z(x)$ (see Eq. 4) was used as a pre-knowledge for the displacement field of the NW in the FEM simulations. FEM model of the bent NW supported by the analytical expression of $u_z(x)$ is presented in Figure 5. Material elastic properties and lattice constants of the NW in FEM simulations were obtained from corresponding GaN bulk material values. Varying parameter $u_{max}$ in the model, the bending limit (maximal displacement in the model that corresponds to gaps appearance in the amplitude distribution) was obtained.

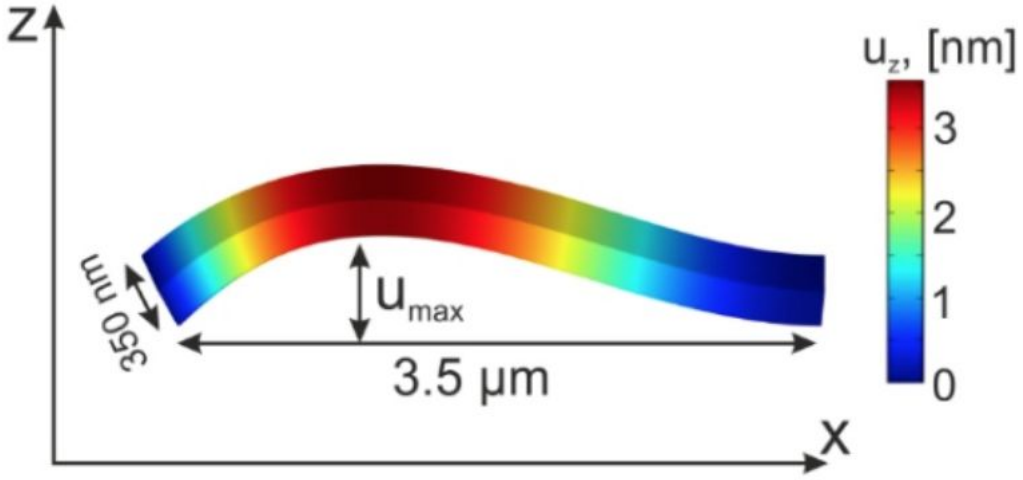


**Figure 5.** Dependence of the displacement component $u_z$ distribution along x coordinate of the nanowire in the FEM model.

## 4. Results and discussion

### 4.1. Real sample

As a first step, reconstruction of the real sample was performed. Diffraction pattern of uncontacted real sample is shown in Figure 6.

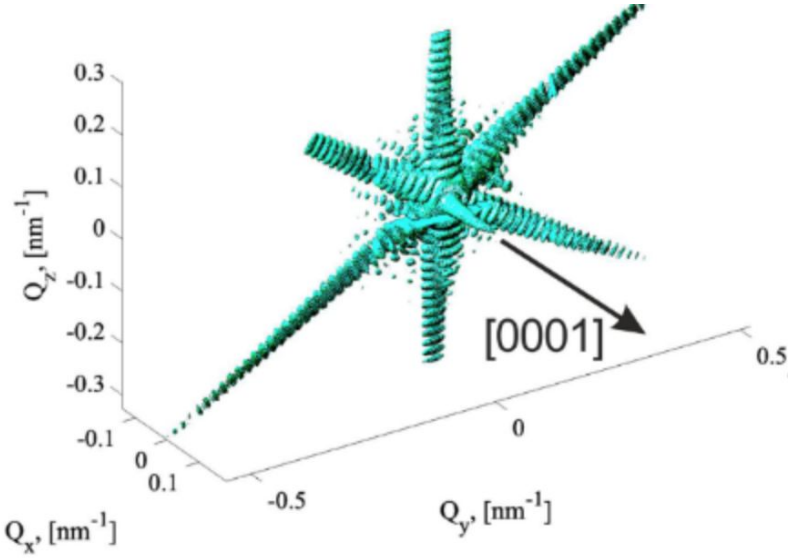


**Figure 6.** 3D diffraction pattern of uncontacted GaN nanowire.

Reconstructed uncontacted nanowire amplitude is presented in Figure 7. The figure shows an average of five performed reconstructions.

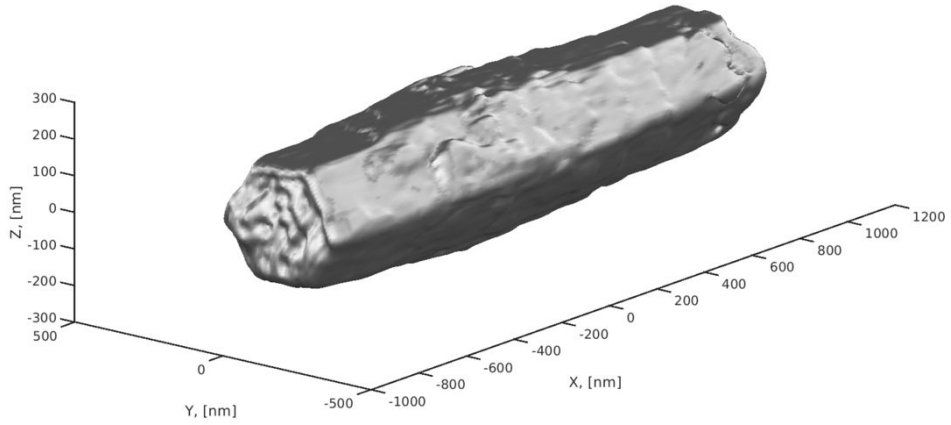


**Figure 7.** Isosurface image of reconstruction of uncontacted GaN nanowire with 0.05 isovalue.

Then, the effect of applied voltage was investigated. In case GaN nanowire is piezoelectric material, increasing of voltage NW leads to bending. Diffraction pattern of the NW under high voltage is show in Figure 8a and amplitude distribution along x direction after reconstruction in the Figure 8b.

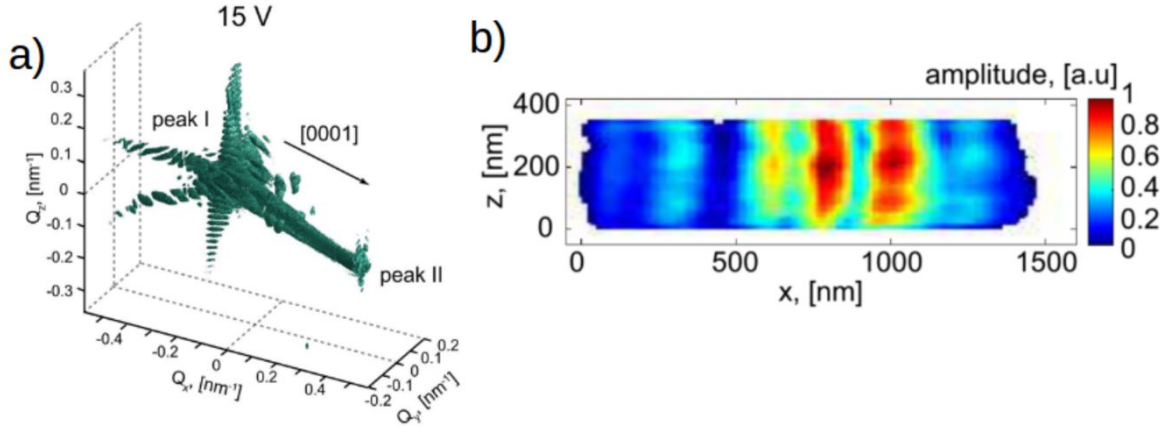


**Figure 8.** a) Diffraction pattern of the GaN nanowire under applied voltage (15 V); b) amplitude distribution along x direction.

Two peeks in Figure 8a correspond to different parts of the bended nanowire. Figure 8b presents the gaps problem. When NW is highly bended, during the reconstruction process, areas of the lower amplitude occur. The bending limit of such regions appearance is the subject of the further discussion.

### 4.2. Model simulation

To simulate how phase retrieval algorithm perform itself in cases with known phase distribution, test sample with even phase distribution from 0 to $\pi$ along z-axis was simulated and reconstructed. In Figure 9 reconstruction of such sample is presented. The CXDI reconstruction is in excellent agreement with the simulated phase distribution.

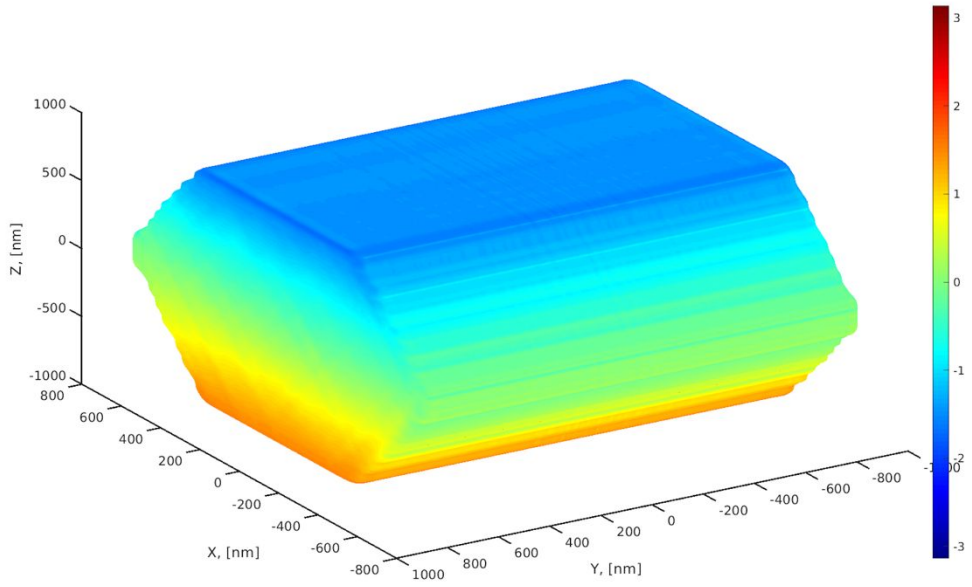


**Figure 9.** Reconstructed object from simulated model with phase distribution along z-axis.

### 4.3. FEM simulation

To investigate bending effect, simulations with FEM model were performed. First, NW with zero phase distribution was simulated and reconstructed as a reference model. In Figure 10 simulated diffraction pattern of the NW (a), NW with phase distribution (b), 3D picture of NW obtained by CXDI (c), phase distribution of central y-axis slice (d) and amplitude distribution of central y-axis slice (e) is shown.

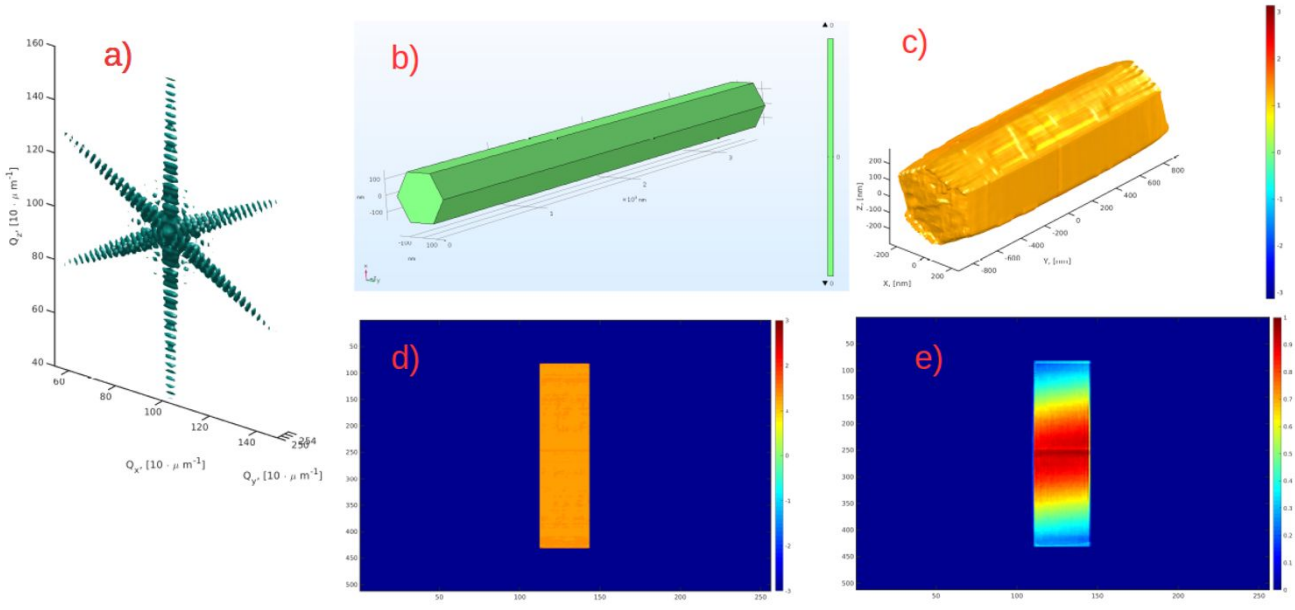


**Figure 10.** Reconstruction of NW simulated with FEM method with zero bending. (a) – diffraction pattern, (b) – initial NW with zero phase distribution, (c) NW reconstructed from the model using CXDI, (d) - phase distribution of central y-axis slice, (e) – amplitude distribution of central y-axis slice.

As it can be seen, CXDI reconstruction reproduce the distribution assigned in the model with small fluctuations. Figure 10e represents effect of Gaussian beam distribution to the amplitude of the object that was applied to the NW with the experimental tilt angle as a part of the modeling process.

Next, simulation with high bending was performed. According to Eq. 6 maximum displacement was chosen to be 3 nm. Diffraction pattern (a) and model of NW with phase distribution (b) is shown in Figure 11. In Figure 12 reconstructed NW with phase distribution is presented.

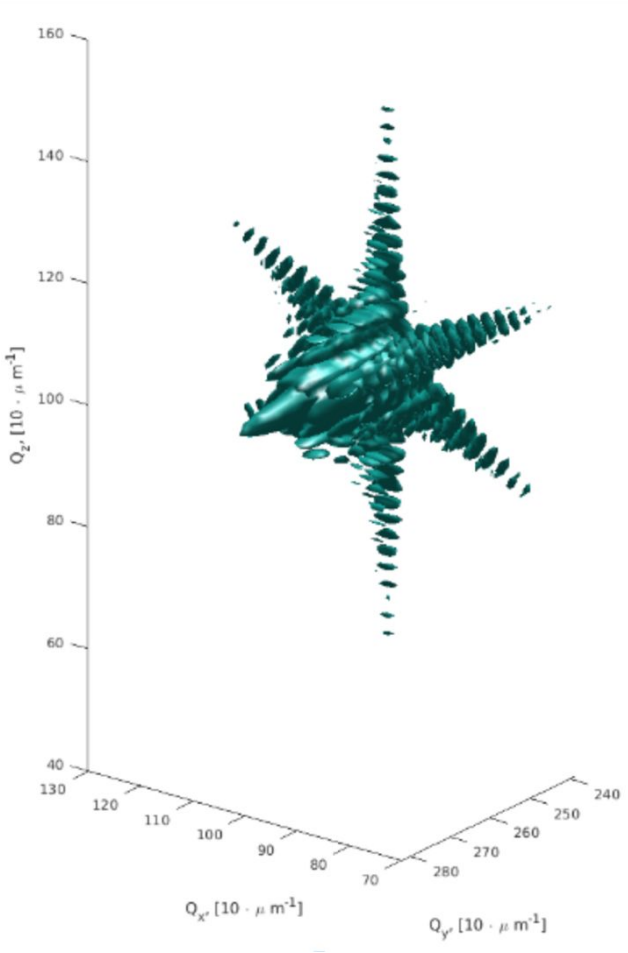


**Figure 11a.** Diffraction pattern of NW with $u_{max} = 3\ nm$.

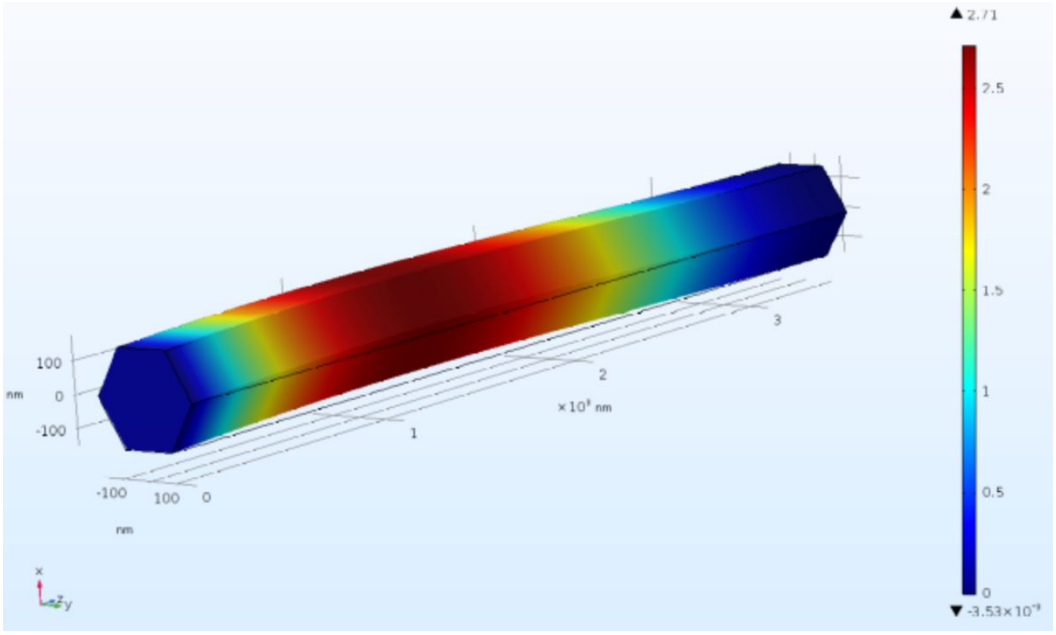


**Figure 11b.** Model of NW with $u_{max} = 3\ nm$.

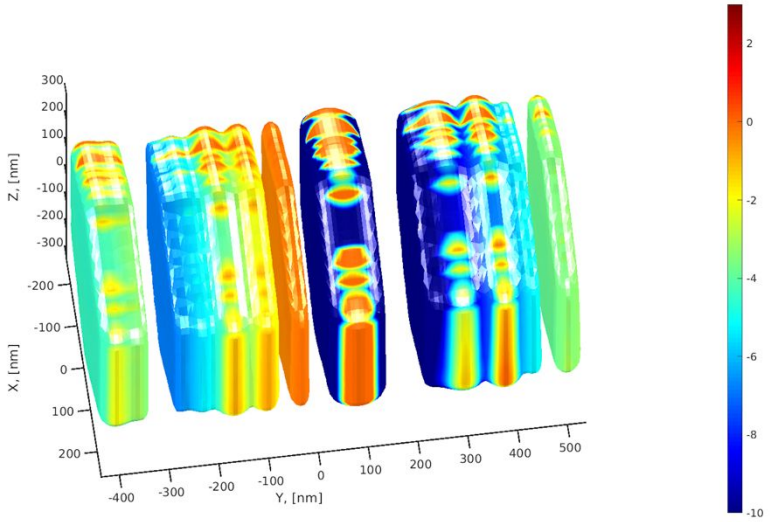


**Figure 12.** Reconstructed NW with $u_{max} = 3\ nm$.

In the reconstruction, several gaps were appeared. It could be considered that $u_{max} = 3\ nm$ is beyond the bending limit. In Figure 13 phase (a) and amplitude (b) distribution of central y-axis slice is introduced.

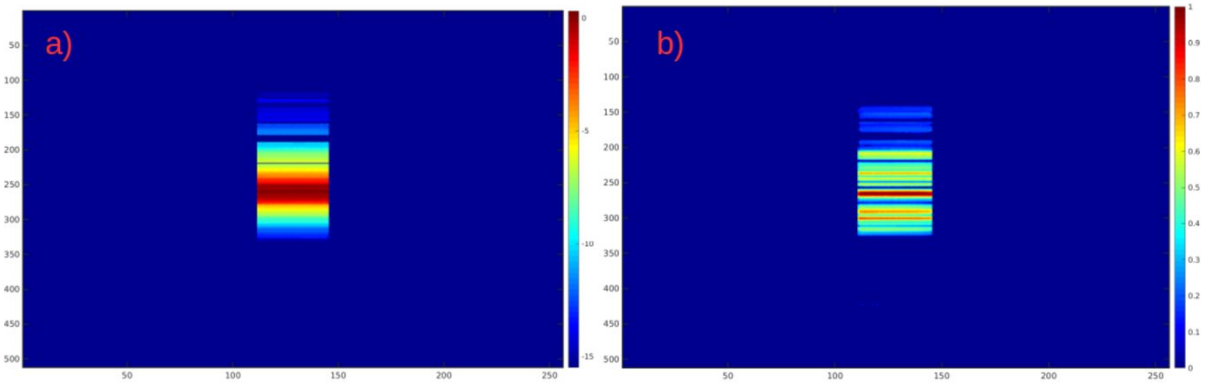


**Figure 13.** Phase (a) and amplitude (b) distribution along central y axis slice of the reconstructed NW with $u_{max} = 3\ nm$.

Next step was to find the point of bending limit of the nanowire. Simulations corresponding to maximum displacement 0.3, 0.6, 0.8 and 1 nm were performed. After executing the reconstruction, the bending limit is found at the 1 nm point of $u_{max}$. FEM model with $u_{max} = 1\ nm$ diffraction pattern is shown in Figure 14a. FEM displacement model with $u_{max} = 1\ nm$ diffraction pattern is shown in Figure 14b. In Figure 15 reconstruction with phase distribution is presented.

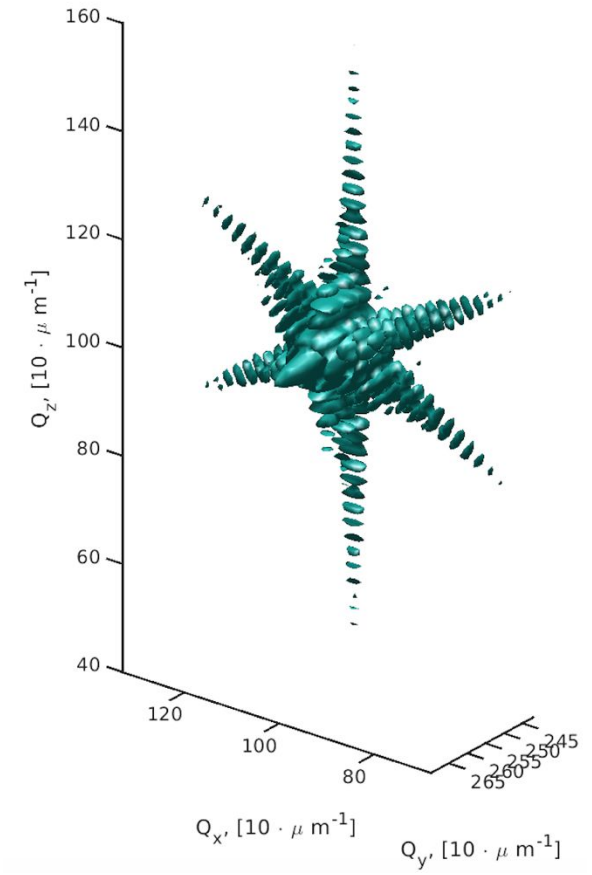


**Figure 14a.**Diffraction pattern of NW with $u_{max} = 1\ nm$ .

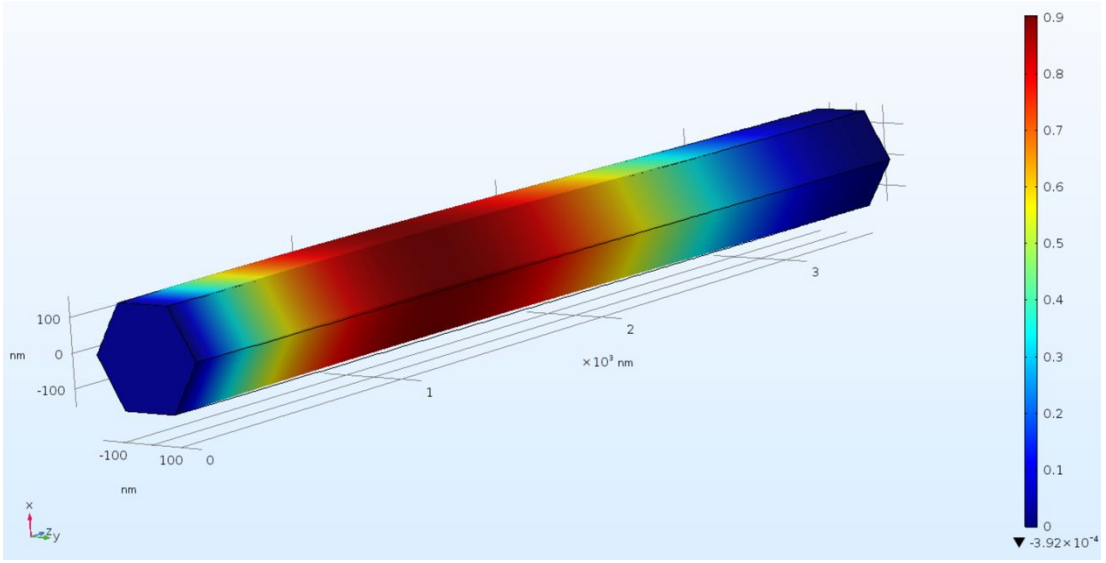


**Figure 14b.** Model of NW with $u_{max} = 1\ nm$ .

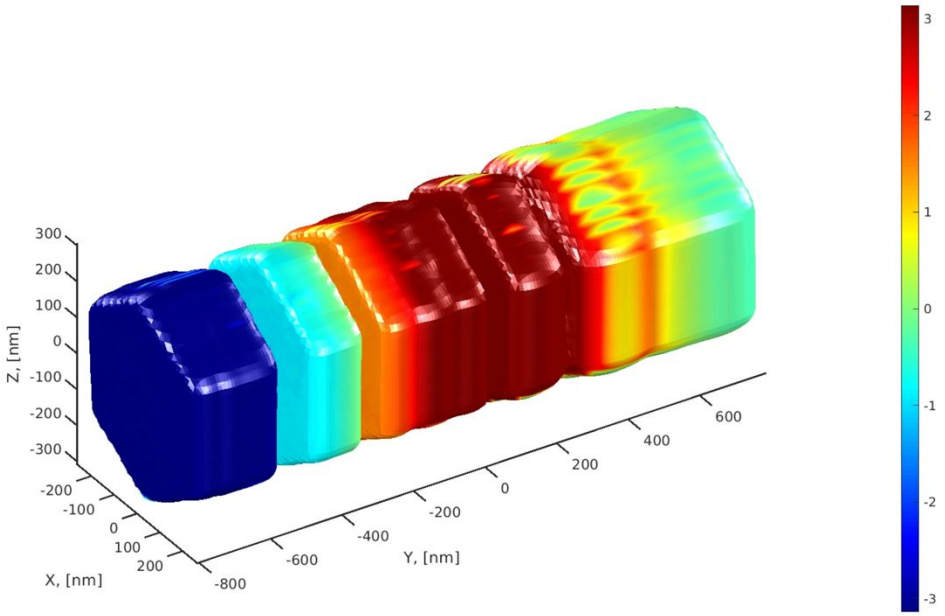


**Figure 15.** Reconstructed NW with $u_{max} = 1\ nm$.

It can be seen that reconstructed structure has gaps. In Figure 16 phase (a) and amplitude (b) distribution of central y-axis slice is introduced. Gaps areas in Figure 15 correspond to low intensity (I < 0.05) regions in Figure 16b where phase can be determined. In this study, such situation is considered as bending limit.

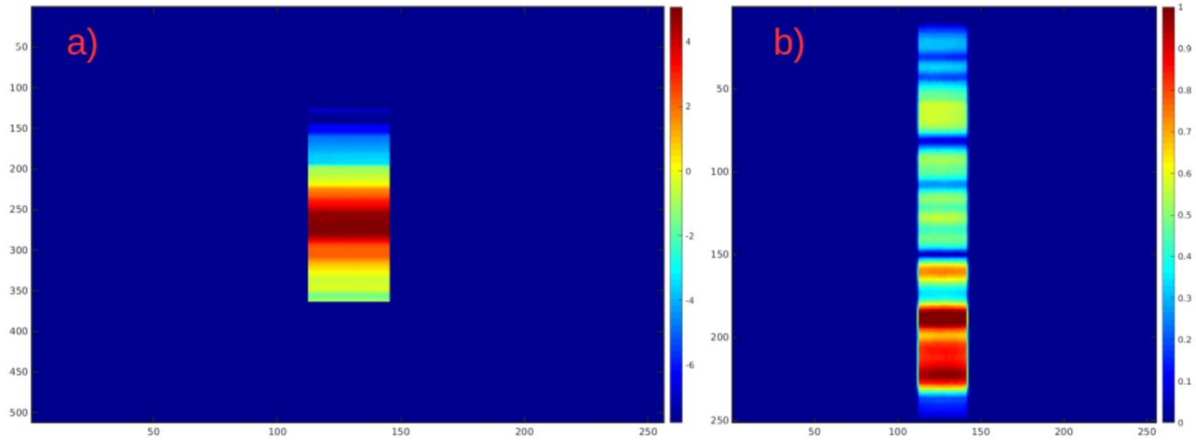


**Figure 16.** Phase (a) and amplitude (b) distribution along central y-axis slice of the reconstructed NW with $u_{max} = 1\ nm$.

Finally, phase retrieval error of the CXDI was estimated. Deviation was evaluated as an average difference between initial phase distribution in the model and reconstructed phase in

the area without phase unwrapping. The dependence of error on maximum displacement of the model is presented in Figure 17.

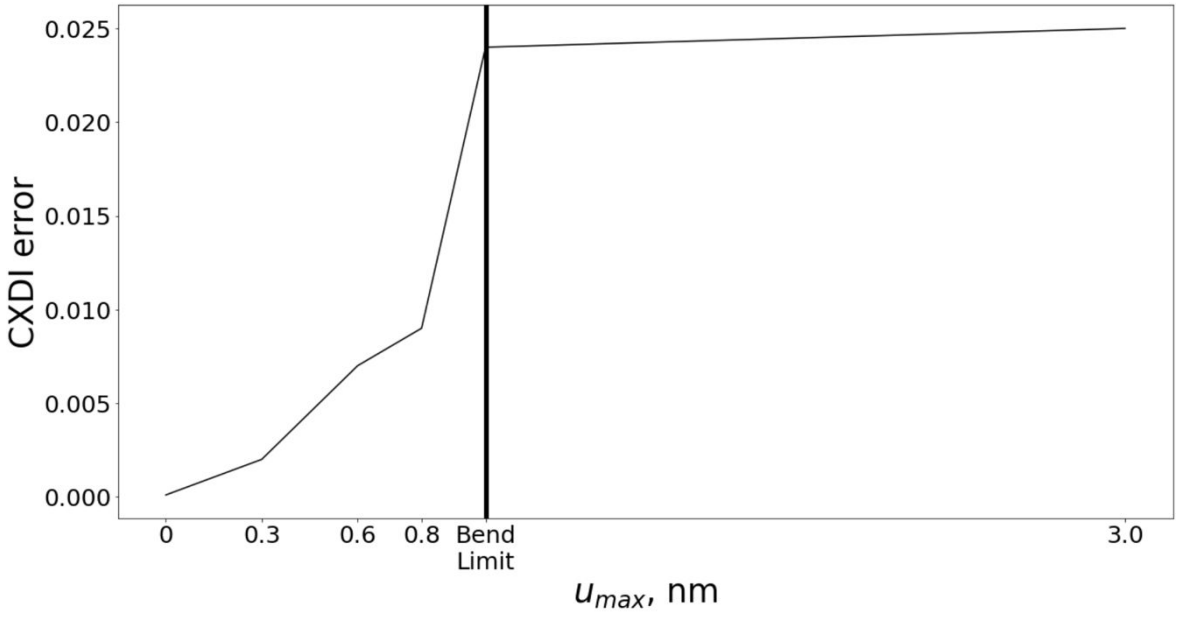


**Figure 17.** Dependence of phase average CXDI error (on pixel) on the maximum displacement $u_{max}$ of the FEM model. Bending limit is show by thick line.

From CXDI error dependence bending limit is also recognized. It corresponds to a model with 1 nm maximum displacement.

## 5. Conclusion

In this work, we studied diffraction patterns of the GaN nanowires. Reconstruction of the real sample was performed. Bended nanowire was explored. It was shown that nanowire under applied voltage had gaps problem that related to the dramatically increasing of displacement. Nanowire with phase distribution along z-axis was reconstructed. FEM models denoted to different maximum displacement were simulated. CXDI reconstructions of the models were in good agreement with initial model. Bending limit that start to appear the gaps was found. The maximum displacement of the model considered to lie in the bended limit is equal to 1 nm. CXDI phase retrieval errors of FEM model reconstructions were calculated. Dependence of the reconstruction error on bending model was presented. From the curve gaps limit was determined. The result is in consistence with the value obtained by reconstruction

analysis. Real bended sample reconstruction, strain constant calculation and solution of gaps problem is plan for further investigation.

## References


1. Li, C.; Wright, J. B.; Liu, S.; Lu, P.; Figiel, J. J.; Leung, B.; Chow, W. W.; Brener, I.; Koleske, D. D.; Luk, T.-S.; Feezell, D. F.; Brueck, S. R. J.; Wang, G. T. Nano Lett. 2017, 17, 1049−1055.
2. Lu, W. Semiconductor Nanowires: From Next-Generation Electronics to Sustainable Energy; The Royal Society of Chemistry, 2014.
3. Feng, Z. C. III-Nitride Materials, Devices and Nano-Structures; World Scientific Publishing Company Pte Limited, 2017.
4. Dasgupta, N. P.; Sun, J.; Liu, C.; Brittman, S.; Andrews, S. C.; Lim, J.; Gao, H.; Yan, R.; Yang, P. Adv. Mater. 2014, 26, 2137−2184. (5) Kuykendall, T.; Ulrich, P.; Aloni, S.; Yang, P. Nat. Mater. 2007, 6, 951−956.
5. Kuykendall, T.; Ulrich, P.; Aloni, S.; Yang, P. Nat. Mater. 2007, 6, 951−956.
6. Huang, C.-T.; Song, J.; Tsai, C.-M.; Lee, W.-F.; Lien, D.-H.; Gao, Z.; Hao, Y.; Chen, L.-J.; Wang, Z. L. Adv. Mater. 2010, 22, 4008−4013.
7. Speck, J. S.; Chichibu, S. F. MRS Bull. 2009, 34, 304−312.
8. Boxberg, F.; Søndergaard, N.; Xu, H. Q. Nano Lett. 2010, 10, 1108−1112.
9. Espinosa, H. D.; Bernal, R. A.; Minary-Jolandan, M. Adv. Mater. 2012, 24, 4656−4675.
10. Minary-Jolandan, M.; Bernal, R. A.; Kuljanishvili, I.; Parpoil, V.; Espinosa, H. D. Nano Lett. 2012, 12, 970−976
11. Muensit, S.; Guy, I. L. Appl. Phys. Lett. 1998, 72, 1896−1898.
12. El Kacimi, A.; Pauliac-Vaujour, E.; Eymery, J. ACS Appl. Mater. Interfaces 2018, 10, 4794−4800.
13. Zhao, Y.; Fu, H.; Wang, G. T.; Nakamura, S. Adv. Opt. Photonics 2018, 10, 246−308.
14. Scholz, F. Semicond. Sci. Technol. 2012, 27, 024002.
15. Speck, J. S.; Chichibu, S. F. MRS Bull. 2009, 34, 304−312.
16. Huang, J. Y.; Zheng, H.; Mao, S. X.; Li, Q.; Wang, G. T. Nano Lett. 2011, 11, 1618−1622.

17. Stankevic, T.; Hilner, E.; Seiboth, F.; Ciechonski, R.; Vescovi, ˇ G.; Kryliouk, O.; Johansson, U.; Samuelson, L.; Wellenreuther, G.; Falkenberg, G.; Feidenhans'l, R.; Mikkelsen, A. ACS Nano 2015, 9, 6978−6984.
18. Stankevic, T.; Dzhigaev, D.; Bi, Z.; Rose, M.; Shabalin, A.; ˇ Reinhardt, J.; Mikkelsen, A.; Samuelson, L.; Falkenberg, G.; Vartanyants, I. A.; Feidenhans'l, R. Appl. Phys. Lett. 2015, 107, 103101.
19. Schroth, P.; Jakob, J.; Feigl, L.; Mostafavi Kashani, S. M.; Vogel, J.; Strempfer, J.; Keller, T. F.; Pietsch, U.; Baumbach, T. Nano Lett. 2018, 18, 101−108.
20. Stankevic, T.; Dzhigaev, D.; Bi, Z.; Rose, M.; Shabalin, A.; ˇ Reinhardt, J.; Mikkelsen, A.; Samuelson, L.; Falkenberg, G.; Vartanyants, I. A.; Feidenhans'l, R. Proc. SPIE 2015, 9592, 95920D−7.
21. Robinson, I. K.; Harder, R. Nat. Mater. 2009, 8, 291−298.
22. Rodenburg, J. M.; Hurst, A. C.; Cullis, A. G.; Dobson, B. R.; Pfeiffer, F.; Bunk, O.; David, C.; Jefimovs, K.; Johnson, I. Phys. Rev. Lett. 2007, 98, 034801.
23. Nugent, K. Adv. Phys. 2010, 59, 1−99
24. Vartanyants, I. A.; Yefanov, O. M. X-ray Diffraction. Modern Experimental Techniques. Coherent X-ray Diffraction Imaging of Nanostructures; Pan Stanford Publishing: Singapore, 2015; Chapter 12, pp 341−384.
25. Newton, M. C.; Leake, S. J.; Harder, R.; Robinson, I. K. Nat. Mater. 2010, 9, 120−124.
26. Godard, P.; Carbone, G.; Allain, M.; Mastropietro, F.; Chen, G.; Capello, L.; Diaz, A.; Metzger, T. H.; Stangl, J.; Chamard, V. Nat. Commun. 2011, 2, 568.
27. Hruszkewycz, S. O.; Holt, M. V.; Murray, C. E.; Bruley, J.; Holt, J.; Tripathi, A.; Shpyrko, O. G.; McNulty, I.; Highland, M. J.; Fuoss, P. H. Nano Lett. 2012, 12, 5148−5154.
28. Dzhigaev, D.; et al. J. Opt. 2016, 18, 064007.
29. Dzhigaev, D.; Stankevic, T.; Bi, Z.; Lazarev, S.; Rose, M.; ˇ Shabalin, A.; Reinhardt, J.; Mikkelsen, A.; Samuelson, L.; Falkenberg, G.; Feidenhans'l, R.; Vartanyants, I. A. ACS Nano 2017, 11, 6605− 6611.
30. Hill, M. O.; et al. Nano Lett. 2018, 18, 811−819.
31. Ulvestad, A.; Singer, A.; Cho, H.-M.; Clark, J. N.; Harder, R.; Maser, J.; Meng, Y. S.; Shpyrko, O. G. Nano Lett. 2014, 14, 5123− 5127.
32. Fienup, J. R. Appl. Opt. 1982, 21, 2758–2769.
33. Marchesini, S.; He, H.; Chapman, H. N.; Hau-Riege, S. P.; Noy, A.; Howells, M. R.; Weierstall, U.; Spence, J. C. H. Phys. Rev. B 2003, 68, 140101.